Degenerate four-wave mixing in THz with standing-wave graphene resonators

THOMAS CHRISTOPOULOS[1,*], ODYSSEAS TSILIPAKOS[2], AND EMMANOUIL E. KRIEZIS[1]

[1]*School of Electrical and Computer Engineering, Aristotle University of Thessaloniki (AUTH), GR-54124 Thessaloniki, Greece*
[2]*Institute of Electronic Structure and Laser, Foundation for Research and Technology-Hellas (FORTH-IESL), GR-71110 Heraklion, Crete, Greece*
[*]*Corresponding author: cthomasa@ece.auth.gr*

Compiled June 25, 2020

Graphene is one the most promising 2D materials for functional electromagnetic components. Harnessing graphene's high third-order nonlinearity, a standing-wave resonant system is proposed that realizes low-power and high-conversion-efficiency degenerate four-wave mixing in the THz regime. The proposed system is analyzed in depth, utilizing a recently developed nonlinear framework based on perturbation theory and temporal coupled-mode theory, which allows for efficient design, accurate results, and physical insight into the system performance. Following robust design guidelines derived from the developed framework, a clear design path is highlighted, covering two possible realizations of the coupling scheme using one or two waveguides as physical ports. The two systems are compared on the basis of input power and conversion efficiency performance metrics, accurately extracted taking into account all relevant nonlinear phenomena including the nonlinear resonance frequency shifts due to self- and cross-phase modulation in graphene, owing to the Kerr effect. The reported values of 10% conversion efficiency and sub-mW power requirements are highly promising for practical applications, highlighting the potential of graphene-based structures in the far-infrared.

OCIS codes: *Nonlinear optics, four-wave mixing (190.4380); Surface plasmons (240.6680); Resonators (230.5750)*

http://dx.doi.org/10.1364/JOSAB.XXXXXX

1. INTRODUCTION

Graphene nowadays is considered as one of the most promising materials for the future of high-functionality photonics, owing to its unique thermal, mechanical, electrical, and optical properties [1]. Especially in the largely unexplored far-infrared (FIR or THz) frequency regime, graphene renewed the interest for functional components, mostly because of its ability to support tightly confined guided modes in the form of graphene surface plasmons (GSPs) [2] and the capability of tuning its properties either electrostatically or optically. Henceforth, GSPs became the basis for the establishment of diverse passive photonic components, such as waveguides [3, 4], resonators [5, 6], and filters [7, 8]. Furthermore, based on the same concept of GSPs, the nonlinear properties of graphene in the FIR have also started to get explored [9–11], leading to the proposition of nonlinear switching [12–15] and frequency generation/mixing elements [16–18], most of which exploit an underlying photonic resonator. The latter provide a field intensity build-up mechanism that enhances light-matter interaction, thus allowing the nonlinear effect to manifest at reduced power levels.

So far, a large body of literature has been published on graphene plasmonics [19–22] exploring interesting functionalities [23–25]; however, advanced functionalities capitilizing for example on the highly nonlinear response of graphene are still at their first steps [26–28]. Towards this goal, here we focus on degenerate four-wave mixing (DFWM) with graphene in the THz regime and study in detail the requirements for obtaining high conversion efficiency with standing-wave resonant structures. Such a systematic approach became feasible due to the recent establishment of a strict and accurate mathematical framework that is capable of handling the DFWM process in triply resonant cavities comprising of arbitrary bulk and sheet-type materials [29–31]. This tool, based on the combination of perturbation theory [32] and temporal coupled-mode theory (CMT) [33], transforms the complex spatiotemporal Maxwell's equations to a much simpler system of coupled, time-dependent, first-order differential equations, providing at the same time physical insight for the resonant system description.

Applying this recently developed framework [29–31], this work aims to provide an in depth comparison of different practical realizations of the DFWM process in standing-wave graphene resonators. Existing works on DFWM with graphene-comprising resonant structures are focused on the NIR [34–37] where graphene does not support surface plasmon polaritons.

In contrast, the context of this work is to examine the far less explored FIR regime where graphene is highly nonlinear and provides the means to tightly confine light through GSP modes. The proposed cavities are designed with care, following a step-by-step approach. We take care to adopt measured material properties, account for all relevant linear and nonlinear phenomena, and conform to fabrication limitations, in order to propose a structure that exhibits high performance metrics and at the same time be as close as possible to a practical realization.

The rest of the paper is organised as follows: In Sec. 2, the mathematical framework that is used throughout the paper is briefly presented and is furthermore applied to extract upper limits for the DWFM performance metrics in standing-wave resonant schemes. Next, in Sec. 3 a physical implementation of a directly-coupled graphene ribbon resonator is presented, with its geometrical parameters being chosen through a design process that provides additional physical insight. The overall performance is thoroughly studied in Sec. 4, where the reliable performance metrics of conversion efficiency and input power requirements are extracted and an intuitive approach to negate the detrimental effect of the Kerr-induced nonlinear frequency shifts that would degrade DWFM efficiency is presented. Finally, Sec. 5 discusses issues regarding the realization of the proposed resonant cavity on a substrate and Sec. 6 concludes our work.

2. NONLINEAR THEORETICAL FRAMEWORK

A. Perturbation theory and coupled-mode theory for multi-channel 2D resonant systems

The resonant elements examined in this work are analysed with an accurate and strict nonlinear framework based on perturbation theory and temporal coupled-mode theory [29, 30], recently expanded to correctly model 2D materials [31]. Under its context, the contribution of any perturbative nonlinearity can be calculated through the general equations [38]

$$\frac{\Delta\omega}{\omega_0} = -\frac{\iiint_V \mathbf{P}_{\mathrm{NL}} \cdot \mathbf{E}_0^* \mathrm{d}V - j\dfrac{1}{\omega_0}\iiint_V \mathbf{J}_{\mathrm{NL}} \cdot \mathbf{E}_0^* \mathrm{d}V}{\iiint_V \dfrac{\partial\left\{\omega\varepsilon_0\overline{\varepsilon}_r + \overline{\sigma}^{(1)}_{\mathrm{Im}}\right\}}{\partial\omega}\mathbf{E}_0 \cdot \mathbf{E}_0^* \mathrm{d}V + \mu_0\iiint_V \mathbf{H}_0 \cdot \mathbf{H}_0^* \mathrm{d}V}, \tag{1}$$

where $\mathbf{P}_{\mathrm{NL}}$ and $\mathbf{J}_{\mathrm{NL}}$ are the perturbative nonlinear polarization and current contributions, $\varepsilon_0\overline{\varepsilon}_r$ is the (real) permittivity tensor, and $\overline{\sigma}^{(1)} = \overline{\sigma}^{(1)}_{\mathrm{Re}} + j\overline{\sigma}^{(1)}_{\mathrm{Im}}$ is the (complex) linear conductivity tensor. Note that the conductivity derivative in the denominator of Eq. (1) is necessary to account for the extra stored energy term, associated with the induced current density [38]; in such cases the equality of electric and magnetic energies on resonance breaks down. The form of Eq. (1) is general and can describe both bulk and sheet nonlinear materials exhibiting any type of nonlinearity, while the tensorial nature of the material linear properties ($\overline{\varepsilon}_r$ and $\overline{\sigma}^{(1)}$) is maintained.

The above equation can be further developed when the nonlinear phenomenon and the underlying materials are specified. In this work, degenerate four-wave mixing in graphene is examined, thus Eq. (1) can be cast in the much simpler form as [29, 31]

$$\Delta\omega_{\mathrm{DFWM},1}\, a_1(t) = -2\beta_1 a_1^*(t) a_2(t) a_3(t), \tag{2a}$$

$$\Delta\omega_{\mathrm{DFWM},2}\, a_2(t) = -\beta_2 a_1^2(t) a_3^*(t), \tag{2b}$$

$$\Delta\omega_{\mathrm{DFWM},3}\, a_3(t) = -\beta_3 a_1^2(t) a_2^*(t), \tag{2c}$$

where the three different $\Delta\omega_k$ quantities are used to describe each involved wave contribution. Furthermore, $a_k(t)$ denotes the respective resonant mode amplitude and $k \in \{1, 2, 3\}$ represents the (strong) pump, the (weak) signal, and the produced idler wave, respectively. The nonlinear parameters β_k (measured in $\mathrm{W}^{-1}\mathrm{s}^{-2}$) are defined for a 2D nonlinear material as [31]

$$\beta_k = \left(\frac{\omega_k}{c_0}\right)^4 \kappa^{\mathrm{DFWM}}_{k,s} \frac{\sigma^{\max}_{3,\mathrm{Im}}}{\varepsilon_0^2}, \tag{3}$$

with $\sigma^{\max}_{3,\mathrm{Im}}$ denoting the spatially maximum value of the $\sigma_{3,\mathrm{Im}}$ parameter, introduced to account for multiple surface materials with different nonlinear properties. The β_k parameters are in general complex and are connected through $\beta_1 = \beta_2^* = \beta_3^*$. As a result, $\Delta\omega_{\mathrm{DFWM},k}$ quantities are also complex to simultaneously model the generation of the new wave due to the nonlinear interactions between the two initial waves, both of which concurrently lose power that is transferred to the generated wave. The nonlinear parameters β_k in turn depend on the *surface nonlinear DFWM feedback parameters*

$$\kappa^{\mathrm{DFWM}}_{1,s} = \left(\frac{c_0}{\omega_1}\right)^4 \frac{\iint_S \sigma_{3,\mathrm{Im}}\, \mathcal{U}_{\mathrm{DFWM}} \mathrm{d}S}{\dfrac{16}{\varepsilon_0^2} W_{\mathrm{res},1} W^{1/2}_{\mathrm{res},2} W^{1/2}_{\mathrm{res},3} \sigma^{\max}_{3,\mathrm{Im}}}, \tag{4a}$$

$$\kappa^{\mathrm{DFWM}}_{2,s} = \left(\frac{\omega_1}{\omega_2}\right)^4 \left(\kappa^{\mathrm{DFWM}}_{1,s}\right)^*, \tag{4b}$$

$$\kappa^{\mathrm{DFWM}}_{3,s} = \left(\frac{\omega_1}{\omega_3}\right)^4 \left(\kappa^{\mathrm{DFWM}}_{1,s}\right)^*, \tag{4c}$$

three parameters that quantify the intensity of the nonlinear process by measuring the modes overlap with the nonlinear material. In this case, only graphene is employed, justifying the reduction to surface integration on the numerators. In Eq. (4a), the following scalar quantity is introduced

$$\mathcal{U}_{\mathrm{DFWM}} = 2(\mathbf{E}^*_{1,\parallel} \cdot \mathbf{E}_{3,\parallel})(\mathbf{E}^*_{1,\parallel} \cdot \mathbf{E}_{2,\parallel}) + (\mathbf{E}^*_{1,\parallel} \cdot \mathbf{E}^*_{1,\parallel})(\mathbf{E}_{2,\parallel} \cdot \mathbf{E}_{3,\parallel}), \tag{5}$$

with the notation $\mathbf{E}_\parallel$ representing the parallel to graphene sheet electric field components; the spatial dependance has been suppressed for brevity. Furthermore, in the denominator of Eq. (4) one can identify the energies stored in each mode in the cavity, defined as [38]

$$\begin{aligned} W_{\mathrm{res},k} =& \frac{1}{4}\iiint_V \left.\frac{\partial\{\omega\varepsilon_0\varepsilon_r\}}{\partial\omega}\right|_{\omega=\omega_k} |\mathbf{E}_k|^2 \mathrm{d}V + \frac{1}{4}\iiint_V \mu_0 |\mathbf{H}_k|^2 \mathrm{d}V \\ &+ \frac{1}{4}\iint_S \left.\frac{\partial\sigma_{1,\mathrm{Im}}}{\partial\omega}\right|_{\omega=\omega_k} |\mathbf{E}_{k,\parallel}|^2 \mathrm{d}S. \end{aligned} \tag{6}$$

Note that the tensorial nature of the underlying materials is either dropped (electric permittivity) or taken into account (graphene complex surface conductivity).

Apart from the DFWM process, the Kerr effect in graphene also affects the resonance frequencies of the cavity. Given the presence of three waves, both self-phase modulation (SPM) and cross-phase modulation (XPM) appear, described through

$$\Delta\omega_{\mathrm{SPM},k}\, a_k(t) = -\gamma_{kk} |a_k(t)|^2 a_k(t), \tag{7a}$$

$$\Delta\omega_{\mathrm{XPM},k\ell}\, a_k(t) = -2\gamma_{k\ell} |a_\ell(t)|^2 a_k(t), \tag{7b}$$

with the nonlinear parameters $\gamma_{k\ell}$ (also measured in $\mathrm{W}^{-1}\mathrm{s}^{-2}$) defined as

$$\gamma_{k\ell} = \left(\frac{\omega_k}{c_0}\right)^4 \kappa_{k\ell,s} \frac{\sigma^{\max}_{3,\mathrm{Im}}}{\varepsilon_0^2}, \tag{8}$$

and the *surface nonlinear SPM/XPM feedback parameters* given by

$$\kappa_{k\ell,s} = \left(\frac{c_0}{\omega_k}\right)^4 \frac{\iint_S \sigma_{3,\mathrm{Im}}\,\mathcal{U}_{k\ell}\,\mathrm{d}S}{\frac{16}{\varepsilon_0^2} W_{\mathrm{res},k} W_{\mathrm{res},\ell}\,\sigma_{3,\mathrm{Im}}^{\max}}. \tag{9}$$

As evident, the parameters $\gamma_{k\ell}$ are real, contrary to β_k. The scalar quantity appearing in Eq. (9) is given by

$$\mathcal{U}_{k\ell} = |\mathbf{E}_{k,\parallel}|^2 |\mathbf{E}_{\ell,\parallel}|^2 + |\mathbf{E}_{k,\parallel}\cdot\mathbf{E}_{\ell,\parallel}|^2 + |\mathbf{E}_{k,\parallel}\cdot\mathbf{E}^*_{\ell,\parallel}|^2. \tag{10}$$

The (complex) resonance frequency shifts of Eq. (2) and Eq. (7) can be readily incorporated in the CMT equations [33]. Assuming a resonant system with three resonances, we can write

$$\begin{aligned}\frac{\mathrm{d}a_k}{\mathrm{d}t} =& j\left(\omega_k - \gamma_{kk}|a_k|^2 - 2\gamma_{k\ell}|a_\ell|^2 - 2\gamma_{km}|a_m|^2\right) a_k \\ & - j\beta_k \Phi_k(a_1,a_2,a_3) - \left(\frac{1}{\tau_{i,k}} + \frac{1}{\tau_{e,k}}\right) a_k + \mu_k s_{\mathrm{in},k}, \end{aligned} \tag{11a}$$

$$s_{\mathrm{tr},k} = c_{t,k} s_{\mathrm{in},k} + d_{t,k} a_k, \tag{11b}$$

$$s_{\mathrm{ref},k} = c_{r,k} s_{\mathrm{in},k} + d_{r,k} a_k. \tag{11c}$$

The resonance amplitudes a_k are normalized so that $|a_k|^2 \equiv W_{\mathrm{res},k}$ express the stored energy on the respective mode, while the wave amplitudes s_k are normalized so that $|s_k|^2 \equiv P_k$ express the guided power in the access waveguides. Furthermore, τ_i and τ_e are the cavity photon lifetimes corresponding to intrinsic (resistive and radiation) and external (coupling) loss, respectively, with the corresponding quality factors given by $Q = \omega\tau/2$. Additionally, to keep the equations general, the quantities μ_k and d_k are introduced, quantifying the coupling from the feeding waveguide(s) to the resonator and vice versa, while the coefficients c_k model the direct path from the input to the transmission/reflection waveguide. All three factors depend on the type of the resonator (standing or traveling wave) and the type of coupling (direct or side coupling) [39]. Finally, the function $\Phi_k(a_1,a_2,a_3)$ appearing in Eq. (11a) is

$$\Phi_k(a_1,a_2,a_3) = \begin{cases} 2a_1^* a_2 a_3, & k=1 \\ a_1^2 a_3^*, & k=2 \\ a_1^2 a_2^*, & k=3 \end{cases}. \tag{12}$$

The CMT equations (11) are usually normalized with respect to the nonlinear phenomenon under study, both for rendering them more easily solvable and to gain physical insight. Choosing the DFWM and specifically the production of the idler wave at ω_3 as the reference phenomenon, the normalization $\tilde{u}_k = (\tau_3|\beta_3|)^{1/2}\tilde{a}_k$ and $\tilde{\psi}_k = \tilde{s}_k/\sqrt{P_3}$ is introduced, with P_3 being the *characteristic power* of the process, defined as

$$P_3 = \frac{\mathcal{A}}{\tau_3^2|\beta_3|}. \tag{13}$$

$\mathcal{A} \in \{1,2\}$, referring to a system that incorporates two/one physical ports, respectively, while in the above definitions $\tau_3 = \tau_{e,3}$ for standing-wave resonators and $\tau_3 = \tau_{i,3}$ for traveling-wave resonators. Note that mode amplitudes and input/transmitted/reflected waves are expressed as $a_k(t) = \tilde{a}_k(t)\exp\{j\omega_k^{\mathrm{op}}t\}$ and $s_k(t) = \tilde{s}_k(t)\exp\{j\omega_k^{\mathrm{op}}t\}$, with ω_k^{op} denoting the operating frequency of the k-th wave that is in general different from the respective resonance frequency of the cavity. In the end, the following system of equations is reached:

$$\begin{aligned}\frac{\tau_k}{\tau_3}\frac{\mathrm{d}\tilde{u}_k}{\mathrm{d}t'} =& -j\delta_k\tilde{u}_k - jr_{\mathrm{SPM},k}|\tilde{u}_k|^2\tilde{u}_k \\ & - j\left(r_{\mathrm{XPM},k\ell}|\tilde{u}_\ell|^2 + r_{\mathrm{XPM},km}|\tilde{u}_m|^2\right)\tilde{u}_k \\ & - jr_{\mathrm{DFWM},k}\Phi_k(\tilde{u}_1,\tilde{u}_2,\tilde{u}_3) - \left(1+r_Q\right)\tilde{u}_k \\ & + \sigma_k\sqrt{\frac{\tau_k}{\tau_3}}\tilde{\psi}_{\mathrm{in},k}, \end{aligned} \tag{14a}$$

$$\tilde{\psi}_{\mathrm{tr},k} = c_{t,k}\tilde{\psi}_{\mathrm{in},k} + \varrho_{t,k}\sqrt{\frac{\tau_3}{\tau_k}}\tilde{u}_k, \tag{14b}$$

$$\tilde{\psi}_{\mathrm{ref},k} = c_{r,k}\tilde{\psi}_{\mathrm{in},k} + \varrho_{r,k}\sqrt{\frac{\tau_3}{\tau_k}}\tilde{u}_k. \tag{14c}$$

The parameters that appear in Eq. (14) are:

- the normalized time $t' = t/\tau_3$,
- the normalized resonance frequencies detuning $\delta_k = (\omega_k^{\mathrm{op}} - \omega_k)\tau_k$,
- the quality factor ratio $r_{Q,k} = \tau_{e,k}/\tau_{i,k}$ for standing-wave resonators (or $r_{Q,k} = \tau_{i,k}/\tau_{e,k}$ for traveling-wave resonators),
- the SPM intensity ratio $r_{\mathrm{SPM},k} = \gamma_{kk}\tau_k/(|\beta_3|\tau_3)$,
- the XPM intensity ratio $r_{\mathrm{XPM},k\ell} = 2\gamma_{k\ell}\tau_k/(|\beta_3|\tau_3)$,
- the DFWM intensity ratio $r_{\mathrm{DFWM},k} = \beta_k\tau_k/(|\beta_3|\tau_3)$,
- the normalized coupling parameters σ_k and ϱ_k, depending on the resonator type and coupling scheme.

The normalized from of Eq. (14) are general, easily solvable, and can apply to any resonant system. Next, we will employ the above framework to evaluate the performance of generic nonlinear standing-wave resonant schemes.

B. Upper performance limits of ideal standing-wave systems

The performance assessment of the system under study begins by examining the ideal case of a generic standing-wave resonator, directly coupled to either one or two physical waveguides, as depicted in Fig. 1(a), (b). This specific type of resonator/coupling scheme is chosen, because it provides the best possible performance based on the relevant literature [29, 30, 40, 41], and is simultaneously suitable for implementing with the GSP platform that is assessed in this work. With the term *ideal* we refer to a system without ohmic and radiation losses ($r_Q = 0$), without self- and cross-phase modulation ($r_{\mathrm{SPM}} = r_{\mathrm{XPM}} = 0$) and with the three consecutive resonance frequencies being equidistant, i.e. by neglecting any material or waveguide dispersion, allowing to set $\delta_k = 0$. For the chosen system, the normalized coupling parameters take the values $\sigma = \{1,2\}$, $\varrho_t = \{1,0\}$, and $\varrho_r = \{1,1\}$ for the double- and single-waveguide configuration, respectively, while $c_t = 0$ and $c_r = -1$ in both cases.

The above parameters are introduced in the CMT framework [Eq. (14)] and the emerging results regarding the conversion efficiency (CE) —the converted idler wave power over the incoming pump and signal waves power, $\mathrm{CE} = 10\log\{p_{\mathrm{out},3}/(p_{\mathrm{in},1}+p_{\mathrm{in},2})\}$— are depicted in Fig. 1(c)-(d) for the two configurations, respectively. There is an ideal point at which CE is maximized. Both its location and its exact value differ between the two configurations, showing that the single-waveguide is advantageous in both pump wave power requirements as well as optimum CE level. Still, both

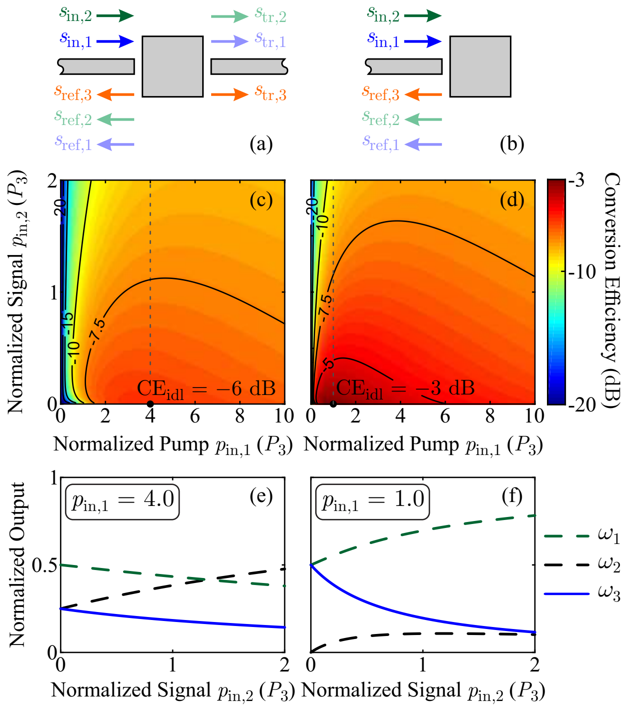

Fig. 1. Schematic of a generic directly coupled, standing-wave resonator with (a) two and (b) one physical port(s). Ideal conversion efficiency map on the $p_{\mathrm{in},1}$-$p_{\mathrm{in},2}$ space, (c) for the double- and (d) for the single-waveguide configuration. The superior performance of the latter is evident. (e)-(f) Normalized power carried by all three outward waves of each configuration as a function of the signal wave power. The pump power level is held constant, as marked in Fig. 1(c)-(d) with a vertical dashed line.

maxima appear when $p_{\mathrm{in},2} \to 0$, revealing that the signal wave is required only for the initiation of the process. We must note here that the incoming power for the two configurations is normalized with respect to a different characteristic power, as evident from the definition in Eq. (13).

The performance is better illustrated after setting $p_{\mathrm{in},1}$ constant and studying the normalized output —the outward power of each wave over the incoming power of both pump and signal waves, $p_{\mathrm{out},k}/(p_{\mathrm{in},1}+p_{\mathrm{in},2})$— with respect to $p_{\mathrm{in},2}$. Note that the term *outward power* refers to the sum of the reflected and transmitted waves power $p_{\mathrm{out},k} = p_{\mathrm{ref},k} + p_{\mathrm{tr},k}$; the latter is nonzero only in the double-waveguide configuration. Beginning from the single-waveguide configuration [Fig. 1(f)], it is easily observed that half of the incoming pump wave power is transferred to the idler wave with the other half remaining at ω_1. The injection of the signal wave only worsens the performance, allowing more power to accumulate at the pump outward direction. For the double-waveguide configuration [Fig. 1(e)], the overall weaker performance is attributed to the fact that half the power created at each wave, and most importantly the signal wave, leaks from the transmission waveguide (right in the schematic).

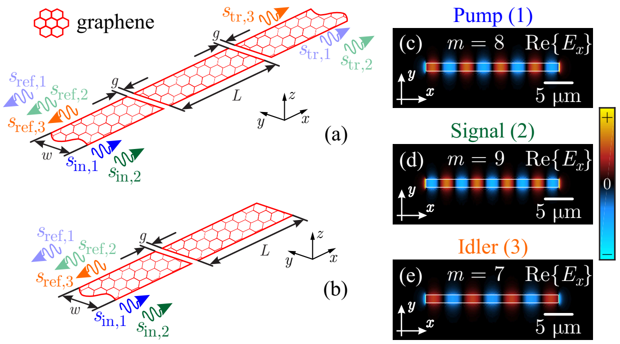

Fig. 2. Schematic of a standing-wave graphene ribbon resonator, directly coupled with (a) two and (b) one bus graphene waveguide(s). (c)-(e) Electric field distribution of the dominant tangential component (E_x) on graphene. Three consecutive modes are depicted, assigned to the (strong) pump, the (weak) signal and the produced idler wave, respectively.

3. GRAPHENE MICRO-RIBBON RESONATOR: PHYSICAL STRUCTURE AND DESIGN

Following the previous discussion, we apply the developed framework to analyze and design a three-dimensional realistic resonant structure, suitable for practical applications, utilizing a graphene ribbon waveguide in the THz frequency regime where tightly confined GSPs are supported [2]. Although the final resonant structure is to be placed on a glass substrate (Sec. 5), in Secs. 3 and 4 we make use of a simplified, free-standing variant to present the design process. The two configurations under study are depicted in Fig. 2(a) and (b), following the generic representation of Fig. 1. The resonant element is a finite length free-standing graphene ribbon waveguide segment, allowing the formation of a standing-wave resonance pattern due to the high reflectivity at the air-graphene interface, introduced by the strong light confinement of the supported GSP mode (the effective index is around 9.5); the supported resonances are of Fabry-Pérot type. This is verified by the resonance pattern of the dominant, tangential to graphene, electric field component, depicted in Fig. 2(c)-(e) for three consecutive resonances of the uncoupled resonator, revealing the quasi-TM nature of the guided plasmons.

Regarding the specifics of the design, the graphene ribbon width is chosen equal to $w = 1$ μm to ensure single-mode operation around 5 THz (free-space wavelength around 60 μm, guided mode wavelength around 6.3 μm), while the length L of the resonator is considered as a design parameter to be specified in what follows. The linear surface conductivity of graphene is calculated from the Kubo formula [42, 43], assuming an achievable Fermi level of $\mu_c = 0.3$ eV and always taking into account the fact that graphene is highly dispersive in the FIR; the choice of the Fermi level renders the conductivity of graphene independent of the exact temperature value, at least under room temperature conditions and for moderate fluctuations of few tens of degrees. Its nonlinear surface conductivity is estimated equal to $\sigma_3 = j1.2 \times 10^{-18}$ S(m/V)^2 [44, 45] for frequencies around 5 THz, corresponding to an equivalent $n_2^{\mathrm{eq}} = 3 \times 10^{-13}$ m^2/W, greatly exceeding typical values of bulk nonlinear materials such as semiconductors, nonlinear polymers, and chalcogenide glasses. It must be noted that $\sigma_3 \propto 1/\omega^3$ is highly dispersive in the FIR but since the employed frequencies are relatively close, we chose to ignore this effect as secondary.

It is important to highlight here how graphene dispersion affects the resonance frequencies spacing, which in an ideal Fabry-Pérot cavity without dispersion are equidistant. To this end, we conduct finite-element (FEM) simulations to calculate the resonance frequencies of three consecutive modes of an $L = 18.1$ μm length graphene ribbon segment. Material dispersion is included by correctly tuning graphene conductivity with respect to the emerging resonance frequency through an iterative procedure, while waveguide dispersion is introduced naturally through the full-wave numerical method (FEM). The resonance frequencies are calculated as $f_3 = 4.36$ THz, $f_1 = 5.00$ THz, and $f_2 = 5.59$ THz, resulting in unequal spacings: $\Delta f_3 = f_1 - f_3 = 0.64$ THz and $\Delta f_2 = f_2 - f_1 = 0.59$ THz. This fact is important in terms of conversion efficiency since, assuming that we choose the initial frequencies to coincide with two of the resonances ($\omega_1^{\mathrm{op}} = \omega_1$ and $\omega_2^{\mathrm{op}} = \omega_2$), then ideally we would like the idler frequency ($\omega_3^{\mathrm{op}} = 2\omega_1^{\mathrm{op}} - \omega_2^{\mathrm{op}}$) to also fall on a resonance frequency ω_3 so that the resonant enhancement of the nonlinear phenomenon is maximized. Only equidistant resonances fulfil this requirement meaning that in dispersive systems $\omega_3^{\mathrm{op}} \neq \omega_3$, limiting the device performance [30, 46]. In CMT terms this fact is reflected in the δ_3 detuning parameter which is nonzero. Note that even when a material with weak inherent dispersion is employed, still waveguide dispersion due to the mode profile changing with frequency induces such detunings. What is more, as found from our simulations, waveguide and material dispersion are of opposite signs, shifting the resonance frequencies towards different directions, thus partly compensating each other. In this specific case, material dispersion dominates over waveguide dispersion, being twice as strong.

The optimum length of the resonator regarding DFWM efficiency can elegantly emerge following a design process which additionally enables a better physical understanding of the resonant system. Initially, we seek to minimize the characteristic power P_3 which is inversely proportional to the $|\kappa_{3,s}^{\mathrm{DFWM}}|Q_{e,3}^2$ product. Therefore, in order to maximize the aforementioned product, we individually examine each involved quantity with respect to the resonator length L. The norm of the nonlinear feedback parameter $\kappa_{3,s}^{\mathrm{DFWM}}$, depicted in Fig. 3(a), decreases with the mode order of the idler wave m_3 because modes of higher order are accompanied by higher effective mode volumes. This results in lower power densities (for a given input power level) and thus weaker electric field amplitudes on graphene. On the contrary, the intrinsic quality factor $Q_{i,3}$, depicted in Fig. 3(b), increases with L since radiation loss is suppressed in longer resonators, until reaching an upper limit set by resistive loss. Interestingly, this increase is not monotonous since even- and odd-order modes radiate differently as the inset of Fig. 3(b) further supports, owing to the phase difference (0 or π rad) between the light in the two opposite physical boundaries of the resonator. However, it is the external and not the intrinsic quality factor that is involved in the calculation of P_3, with its value depending exclusively on the coupling gap g between the resonator and the bus waveguide(s). High $Q_{e,3}$ values are on one hand desirable because they lead to lower P_3. On the other hand though, they worsen the conversion efficiency due to the higher $r_{Q,3}$ factors introduced [31]. As a compromise, we choose $r_{Q,3} = 0.2$ and consequently depict the resulting $Q_{e,3}$ values on Fig. 3(b) as well. Because the quality factors smoothly change with L, the values of P_3 [Fig. 3(c)] monotonically increase; in this sense, shorter resonators are preferable.

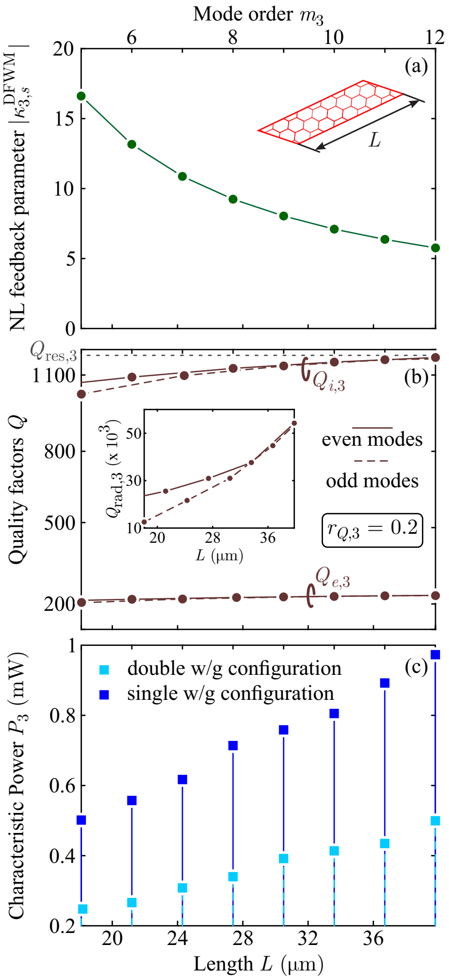

Fig. 3. (a) Nonlinear DFWM feedback parameter $|\kappa_{3,s}^{\mathrm{DFWM}}|$ versus mode order of the idler wave m_3. (b) Intrinsic $Q_{i,3}$ and external $Q_{e,3}$ quality factors versus m_3. Inset: radiation quality factor $Q_{\mathrm{rad},3}$ versus m_3. (c) System characteristic power P_3 versus m_3 at $r_{Q,3} = 0.2$. The opposite trends in $|\kappa_{3,s}^{\mathrm{DFWM}}|$ and $Q_{e,3}$ do not result in a local minimum on P_3 because of the small slope of the $Q_{e,3}$ curve. All quantities are discrete; the solid/dashed lines are used as a guide to the eye.

Nevertheless, in all cases considered the power requirements are in the sub-mW regime. Finally, it must be noted that the characteristic power of the double-waveguide configuration is half that of the single-waveguide system, exclusively owing to its definition [parameter $\mathcal{A}$ in Eq. (13)]. Still, because P_3 is only a quantitative measure of the necessary input power for a nonlinear phenomenon to develop, this twofold difference is not necessarily important at this point.

Next, the induced frequency mismatch between the resonance and the produced idler wave from the operating frequencies is examined in Fig. 4(a). The parameter δ_3 (positive in this case) which quantifies the aforementioned effect decreases with L for both configurations. This behaviour is expected since the resonator free-spectral rance (FSR) —estimated through $\mathrm{FSR} = c_0/2n_{\mathrm{eff}}(\omega)L$, with $n_{\mathrm{eff}}(\omega)$ representing the effective index of the supported GSP mode— is inversely proportional to L. Thus, the three resonances associated with the pump, signal, and idler waves are approaching each other, limiting the

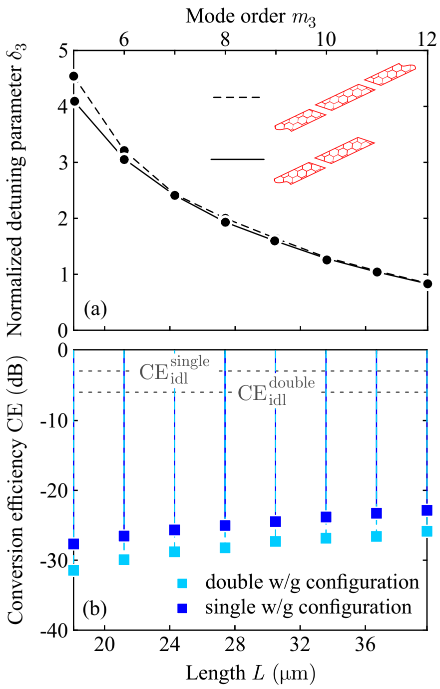

Fig. 4. (a) Normalized detuning parameter δ_3 versus mode order of the idler wave m_3. It is calculated assuming $\omega_1^{\mathrm{op}} = \omega_1$ and $\omega_2^{\mathrm{op}} = \omega_2$, so that $\delta_3 = (\omega_3^{\mathrm{op}} - \omega_3)\tau_{e,3}$. (b) Maximum conversion efficiency (including SPM/XPM) versus m_3. Maximum CE monotonically raises with m_3, attributed to the lower δ_3 values which suppress the impact of dispersion. All quantities are discrete; the solid/dashed lines are used as a guide to the eye.

effect of material and waveguide dispersion. Note here that the parameter δ_3 is calculated using the *coupled* resonance frequencies of the respective configuration in order to take into account the coupling-induced frequency shift (CIFS) [47]. CIFS in the double-waveguide configurations is slightly stronger for lower order modes because of the employment of two waveguides that both slightly disturb the field distribution in the vicinity of the coupling regions. In higher order modes, this effect is not as pronounced.

The fact that longer resonators are associated with lower δ_3 detunings is expected to enhance the maximum conversion efficiency of the respective structure. This is indeed the case in Fig. 4(b), which depicts the maximum achievable CE values when SPM and XPM are taken into account. The results verify that maximum CE increases with L due to the smaller δ_3 values. The large distance from the ideal upper limits specified in Sec. 2 B [depicted with horizontal lines, reflecting the findings of Fig. 1(c) and (d)] is due to the presence of SPM/XPM [31]. Additionally, the single-waveguide configuration outperforms the double one by exactly 3 dB in any given case with $\delta_1 = \delta_2 = 0$, as expected from the results of Fig. 1(c)-(f). The presented CE is calculated using the developed CMT framework, fed with the respective linear and nonlinear parameters calculated by means of FEM eigenvalue simulations. Extra details can be found in the next section. Finally, note that in the double-waveguide system, the idler wave power is calculated using the outward power (sum of both transmission and reflection powers).

Based on the results presented thus far, a preferable operation point can be found by jointly considering the two opposite trends on P_3 and CE [cf. Fig. 3(c) and Fig. 4(b)] for either of the two configurations. Towards that goal, we plot in Fig. 5 the necessary input power to reach the maximum CE in each examined scenario. It is clear that both for the double- and the single-waveguide configuration there exists a minimum in the necessary input power of the pump wave at which maximum CE is observed. Notably, this minimum is the same for both configurations and specifically it is reached for an $L = 24.3$ μm long resonator, supporting the $m_3 = 7$ order mode which is appointed to the produced idler wave. What is more, because δ_3, r_Q, r_{SPM}, and r_{XPM} are all nonzero, the signal wave input power to reach maximum CE should be nonzero as well. Nevertheless, it is almost invariable with L and in any case lower than that of the pump wave; thus we do not seek on minimizing it as well. We find that between the two configurations the single-waveguide one is advantageous, requiring lower input power and leading to higher conversion efficiency. In particular, for the double-waveguide configuration we get $P_{\mathrm{in},1} = 240$ μW and $P_{\mathrm{in},2} = 132$ μW with $\mathrm{CE}_{\max} = -28.8$ dB, while for the superior, single-waveguide design the respective power quantities are almost halved, $P_{\mathrm{in},1} = 127$ μW and $P_{\mathrm{in},2} = 77$ μW, and at the same time $\mathrm{CE}_{\max} = -25.8$ dB is doubled.

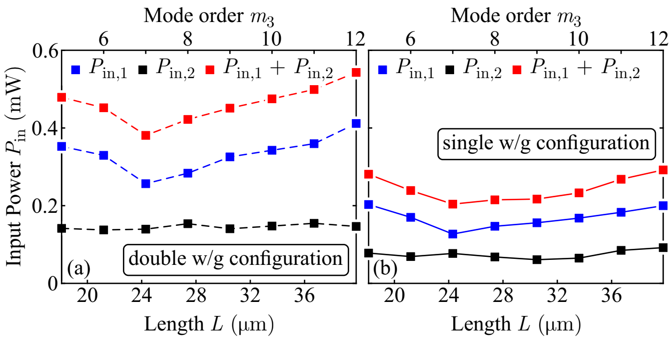

Fig. 5. Necessary input power for both pump and signal waves to reach the maximum conversion efficiency versus mode order of the idler wave m_3. (a) Double- and (b) single-waveguide configuration. For both scenarios, the optimum operating resonator length is $L = 24.3$ μm. The superiority of the single-waveguide configuration is evident.

Given the choice of $r_{Q,3} = 0.2$, we can finally calculate the coupling gap between the resonator and the bus waveguide(s). In the double-waveguide configuration, this leads to $g = 0.43$ μm which, in turn, results in $r_{Q,1} = 0.23$ and $r_{Q,2} = 0.26$, given that the coupling efficiency is different between different order modes. In the single-waveguide configuration, the respective gap is found equal to $g = 0.23$ μm, leading to $r_{Q,1} = 0.22$ and $r_{Q,2} = 0.24$. The smaller gap in the latter case is a direct reflection of the fact that the same amount of power must escape from a single waveguide rather than from the two of the former case. Overall, the resonance frequencies, the quality factors and the nonlinear parameters for all three modes of each configuration are compiled in tables 1 and 2. The resonance frequencies are all calculated for the coupled system to take CIFS into account. Additionally, the *intrinsic* quality factors are also calculated using the *coupled* system to correctly exclude the radiation that is associated with the evanescent coupling to the bus waveguide(s) [48]. The latter justifies the small differences in the intrinsic Q-factor between the two configurations (table 1).

Table 1. Linear parameters calculated via the eigenvalue FEM simulations and used in the CMT framework.

Double-waveguide configuration			
$m_1 = 8$	$f_1^c = 4.9988$ THz	$Q_{i,1} = 1\,234$	$Q_{e,1} = 279$
$m_2 = 9$	$f_2^c = 5.4466$ THz	$Q_{i,2} = 1\,338$	$Q_{e,2} = 343$
$m_3 = 7$	$f_3^c = 4.5264$ THz	$Q_{i,3} = 1\,097$	$Q_{e,3} = 221$
Single-waveguide configuration			
$m_1 = 8$	$f_1^c = 4.9989$ THz	$Q_{i,1} = 1\,231$	$Q_{e,1} = 265$
$m_2 = 9$	$f_2^c = 5.4467$ THz	$Q_{i,2} = 1\,334$	$Q_{e,2} = 314$
$m_3 = 7$	$f_3^c = 4.5265$ THz	$Q_{i,3} = 1\,094$	$Q_{e,3} = 221$

Table 2. Nonlinear parameters calculated via the eigenvalue FEM simulations and used in the CMT framework.

Double-waveguide configuration				
	$r_{\mathrm{SPM},k}$	$r_{\mathrm{XPM},k\ell}$	$r_{\mathrm{XPM},km}$	$r_{\mathrm{DFWM},k}$
$k = 1$	2.61	4.12	2.85	$1.06 + j0.43$
$k = 2$	3.21	3.60	2.95	$1.19 - j0.49$
$k = 3$	2.07	3.36	3.99	$0.93 - j0.38$
Single-waveguide configuration				
	$r_{\mathrm{SPM},k}$	$r_{\mathrm{XPM},k\ell}$	$r_{\mathrm{XPM},km}$	$r_{\mathrm{DFWM},k}$
$k = 1$	2.49	3.93	2.71	$1.01 + j0.41$
$k = 2$	2.95	3.30	2.71	$1.09 - j0.45$
$k = 3$	2.07	3.36	3.99	$0.93 - j0.38$

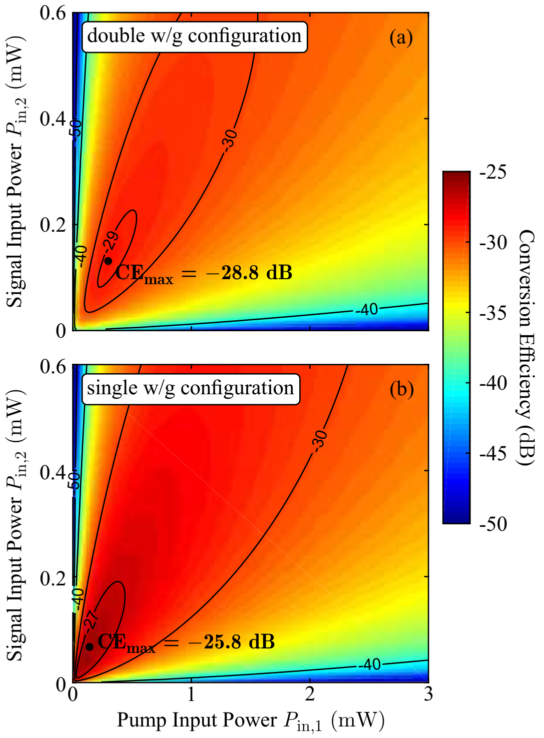

Fig. 6. Conversion efficiency metric in the $P_{\mathrm{in},1}$-$P_{\mathrm{in},2}$ space for $\delta_1 = \delta_2 = 0$. (a) Double- and (b) single-waveguide configuration. A maximum is observed in both cases with the latter being optimal both in terms of CE and P_{in}.

4. PERFORMANCE EVALUATION UNDER SPM/XPM

Having determined the physical dimensions of the device under study and the parameters that describe it, in this section we move to a more exhaustive examination and evaluation of the two configurations performance. The analysis begins by setting $\delta_1 = \delta_2 = 0$ and examining the CE metric in the $P_{\mathrm{in},1}$-$P_{\mathrm{in},2}$ space. As evident from Fig. 6, both configurations exhibit a maximum CE point. Thus, it is indeed verified that the single-waveguide configuration outperforms the double one, both in terms of maximum conversion efficiency and in input power requirements.

The maximum conversion efficiency remains relatively low, being comparable with those of straight waveguide alternatives [49–51], which are more fabrication friendly. Although resonant structures can be advantageous in terms of performance due to the light intensity build up they provide, so far this enhancement effect has been suppressed by the nonlinear frequency shifts induced by SPM and XPM. However, CE can be restored in its original high levels by (partly) negating the SPM/XPM contribution after appropriately pre-shifting the operating frequencies so that when SPM/XPM manifest, the operating and the shifted resonance frequencies will coincide [29, 52]. Although the estimation of the pre-shift can be performed analytically [52], we choose to follow a more instructive path by keeping the input powers in their optimum levels and performing a parametric analysis in the δ_1-δ_2 space. The results of the parametric analysis are depicted in Fig. 7. As can be seen, at least a 15 dB enhancement is achievable only by correctly choosing the operating frequencies. More specifically, an optimum $\mathrm{CE_{opt}} = -14.2$ dB is achieved in the double-waveguide configuration when $\delta_1 = -3.5$ and $\delta_2 = -2.0$, resulting in $\delta_3 = -2.2$. On the other hand, even better performance is obtained for the single-waveguide configuration, with $\mathrm{CE_{opt}} = -8.5$ dB when $\delta_1 = -4.4$ and $\delta_2 = -2.1$, resulting in $\delta_3 = -3.7$. The final +17.4 dB enhancement, achieved only by correctly choosing the operating frequencies is rather impressive. In terms of physically understandable quantities, the operating frequencies are chosen as $f_1^{\mathrm{op}} = 4.9575$ THz, $f_2^{\mathrm{op}} = 5.4285$ THz, and thus $f_3^{\mathrm{op}} = 4.4865$ THz, slightly red-shifted from the coupled resonance frequencies of table 1. The 5.5 dB missing to reach the ideal CE limit cannot be recovered because of graphene losses and dispersion (material and waveguide) that cannot be canceled out.

In the detuning parameters space, we have marked unstable regions where the phenomenon of optical bistability (BI) establishes [14, 31], owing either to SPM or to XPM. These regions exist when at least one δ parameter is negative since SPM and/or XPM in graphene red-shift the resonance frequencies. Nevertheless, the maximum CE point is not surpassed in any of the two possible bistable states, as we have found from the simulations conducted. To validate the bistable response, in Fig. 7(c) we examine the temporal response of an operating point lying inside a bistable region in the single-waveguide configuration, marked with a red star in Fig. 7(b). The system is initially in a low efficiency state, but after injecting an appropriate triangular pulse in the pump wave, the second, high-CE state is reached. The system is restored in its initial state after a second triangu-

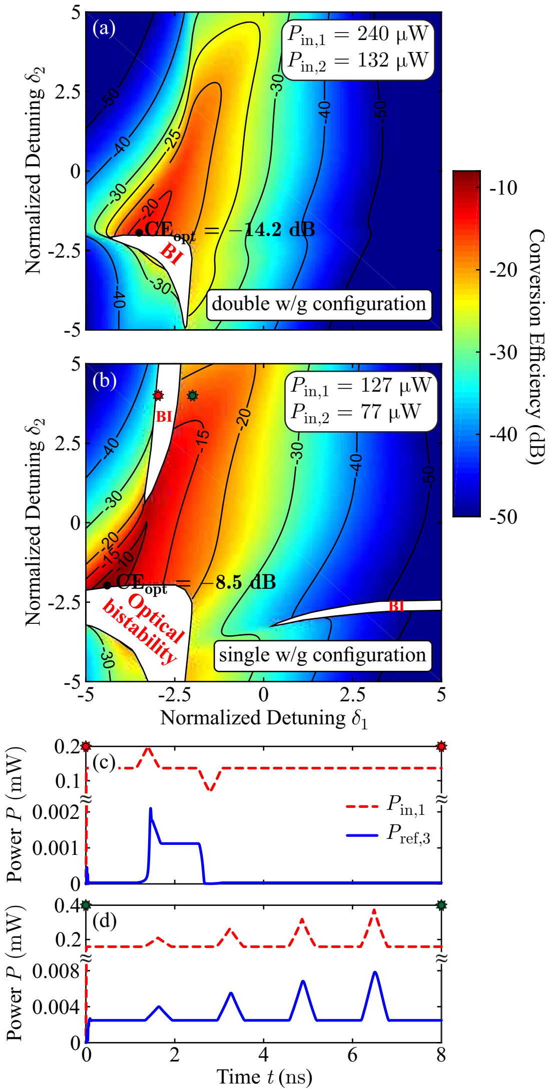

Fig. 7. Conversion efficiency metric in the δ_1-δ_2 space for the optimum input powers emerging from Fig. 6. (a) Double- and (b) single-waveguide configuration. An important enhancement is obtained for both configurations, with the single-waveguide one having again the best performance, reaching a CE$_{opt}$ = −8.5 dB. (c) Detailed examination of the bistable behaviour in the red star-marked point of Fig. 7(b), lying inside a bistability region. (d) Verification of the absence of bistability in the green star-marked point of Fig. 7(b). (BI: Optical Bistability)

lar pulse with a different sign is injected; a clear indication of classic bistable behaviour [53]. On the contrary, a point lying in a stable area exhibits a clearly stable response; injecting triangular pulses with various amplitudes cannot trigger a transition to a different output state [Fig. 7(d)]. Note that for both the examined cases, the input power of the signal wave is kept constant at $P_{in,2} = 77\ \mu$W.

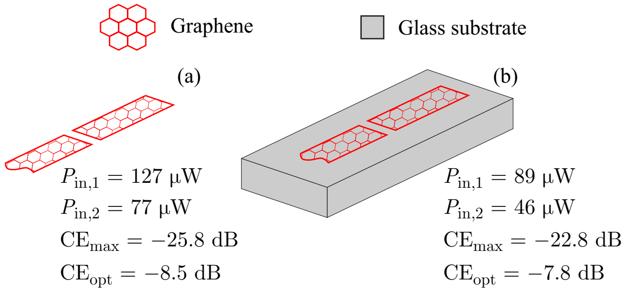

Fig. 8. Device implementation alternatives and their final performance: (a) The so far examined air-standing graphene ribbon. (b) Graphene ribbon on a glass substrate.

5. FINAL RESONANT SYSTEM ON GLASS SUBSTRATE

We now place the previously evaluated graphene ribbon on top of a glass substrate with a typical refractive index of $n_{sub} \sim 1.5$. Although the relaxation time of graphene and the Fermi level might vary considerably depending on the presence of the substrate and the fabrication process (direct growth or transfer of the graphene mono-layer) here we choose to retain the same values throughout. The exact performance and reported values of conversion efficiency might vary according to the actual fabricated structure; however, the design methodology and the phenomena that need to be considered for specifying the optimum operating point remain unchanged. The length of the ribbon is kept constant and the system is evaluated with respect to the characteristic power and the emerging frequency detuning of the idler wave. For the glass-substrate configuration, the above quantities are calculated equal to $P_3 = 577\ \mu$W (single-waveguide system definition) and $\delta_3 = +1.41$, respectively. For comparison, the corresponding values of the air-suspended graphene are $P_3 = 618\ \mu$W and $\delta_3 = +2.41$. The better performance of the glass substrate configuration is attributed to the higher effective index that the supported modes exhibit (13.3 versus 9.5), thus allowing the establishment of higher order modes for the same resonator length ($m \propto n_{eff}$), which are characterized by higher quality factors and, despite the lower κ parameters, by slightly better metrics in terms of power requirements due to lower radiation loss. Although one might suggest that comparing modes of different order is unfair, still examining the same order modes of the air-suspended ribbon (assuming it has a longer length), results in worse performance metrics regarding P_3 because of the lower mode confinement (lower κ values) and the fact that the quality factors are the same (radiation is of equal intensity between the two scenarios).

The final performance metrics regarding the actual input power requirements and the maximum conversion efficiencies before and after SPM/XPM compensation are also gathered in Fig. 8. Specifically, the glass substrate configuration exhibits a compensated maximum conversion efficiency of CE = −7.8 dB, achievable for input power requirements below 100 μW: $P_{in,1} = 89\ \mu$W and $P_{in,2} = 46\ \mu$W. Overall, the final performance metrics are considered as very high while the structural complexity of the resonant element is maintained low so that its physical realization remains realistic.

6. CONCLUSION

To recapitulate, in this work we have demonstrated efficient degenerate four-wave mixing in directly coupled graphene standing-wave resonators, suitable for practical applications in the THz. Employing our efficient and accurate framework that allows to analyze resonant structures supporting DFWM that involve 2D photonic materials, we have highlighted the design requirements and considerations of such devices for efficient,

Table 3. Comparison of the current work with state-of-the-art devices for DFWM in the FIR and the NIR frequency regimes.

Platform	System	Method	Idler Frequency	CE	Input Powers $P_p + P_s$	Reference
Gr	Resonator	Theory	4.5 THz	-7.8 dB	$(89 + 46)$ μW	This work
Si	Waveguide	Theory	32 THz	-20.8 dB	$(2000 + 1000)$ W^a	[54]
PhC w/ Gr (edge waves)	Waveguide	Theory	12 THz	< -20 dB^b	$(5 + 0.0005)$ nW	[28]
Patterned Gr	Metasurface	Theory	3.1 THz	-8.2 dB^c	$(30 + 30)$ kW/cm^2	[55]
Gr on Si	Waveguide	Theory	NIR	-30 dB	$(500 + 0.25)$ mW	[50]
Gr on Si	Resonator	Experiment	NIR	-38 dB	$(8 + 1)$ mW	[35]
GO on SiO$_2$	Resonator	Experiment	NIR	-38 dB	$(160 + 160)$ mW	[56]
MoS$_2$ on Si	Waveguide	Experiment	NIR	-32.1 dB	$(1 + 0.1)$ mW	[57]

[a] Peak pulse power, [b] Lossy case, -3.2 dB for the lossless case, [c] Extracted from the manuscript reported values.

low-power operation. Such an approach was made available through the perturbation theory/coupled-mode theory framework, which provides extra physical insight owing to the mathematically straightforward modeling equations and also allows for quick and meticulous calculations of the nonlinear process metrics.

A methodical analysis and design procedure has been followed, starting from the ideal scenario (absence of dispersion and losses) of an abstract standing-wave resonator under two different coupling configurations. The findings were subsequently used to guide the design steps of a more practical 3D graphene ribbon resonator, which geometrical parameters have been specified on the basis of optimizing the power requirements and conversion efficiency. Throughout the process, the two coupling configurations are comparatively assessed; we found that the single-waveguide variant is advantageous in terms of all performance metrics. Importantly, the dramatic effect of SPM/XPM on the CE suppression is highlighted, while an approach to partly negate their effect is presented, simply by correctly detuning the operating frequencies with respect to the resonance frequencies. This allows for approaching the ideal values of conversion efficiency and harnessing the full potential of resonant structures for nonlinear applications, inherited from the intensity build-up they provide. The final performance of CE $= -7.8$ dB with $P_{\text{in}} = 135$ μW highlights the potential of graphene as a nonlinear material for THz applications, as the accompanying Table 3 also reveals, gathering the state-of-the-art works on DFWM with resonant and waveguiding structures, incorporating graphene or other 2D materials on contemporary material platforms.

Funding. Hellenic Foundation for Research and Innovation (H.F.R.I.), Project Number: HFRI-FM17-2086

Acknowledgments. The research work was supported by the Hellenic Foundation for Research and Innovation (H.F.R.I.) under the “First Call for H.F.R.I. Research Projects to support Faculty members and Researchers and the procurement of high-cost research equipment grant.” (Project Number: HFRI-FM17-2086)

Disclosures. The authors declare no conflicts of interest.

REFERENCES

1. K. S. Novoselov, V. I. Fal’ko, L. Colombo, P. R. Gellert, M. G. Schwab, and K. Kim, “A roadmap for graphene,” Nature **490**, 192–200 (2012).
2. Y. V. Bludov, A. Ferreira, N. M. R. Peres, and M. I. Vasilevskiy, “A primer on surface plasmon-polaritons in graphene,” International Journal of Modern Physics B **27**, 1341001 (2013).
3. J. Zheng, L. Yu, S. He, and D. Dai, “Tunable pattern-free graphene nanoplasmonic waveguides on trenched silicon substrate,” Scientific Reports **5**, 7987 (2015).
4. M. Hajati and Y. Hajati, “Investigation of plasmonic properties of graphene multilayer nano-ribbon waveguides,” Applied Optics **55**, 1878–1884 (2016).
5. L. Zhang, J. Yang, X. Fu, and M. Zhang, “Graphene disk as an ultra compact ring resonator based on edge propagating plasmons,” Applied Physics Letters **103**, 163114 (2013).
6. H.-J. Li, L.-L. Wang, B. Sun, Z.-R. Huang, and X. Zhai, “Tunable mid-infrared plasmonic band-pass filter based on a single graphene sheet with cavities,” Journal of Applied Physics **116**, 224505 (2014).
7. J. S. Gómez-Díaz and J. Perruisseau-Carrier, “Graphene-based plasmonic switches at near infrared frequencies,” Optics Express **21**, 15490–15504 (2013).
8. H. Zhuang, F. Kong, K. Li, and S. Sheng, “Plasmonic bandpass filter based on graphene nanoribbon,” Applied Optics **54**, 2558–2564 (2015).
9. S. A. Mikhailov, “Non-linear electromagnetic response of graphene,” Europhysics Letters (EPL) **79**, 27002 (2007).
10. B. Semnani, A. H. Majedi, and S. Safavi-Naeini, “Nonlinear quantum optical properties of graphene,” Journal of Optics **18**, 035402 (2016).
11. H. Rostami, M. I. Katsnelson, and M. Polini, “Theory of plasmonic effects in nonlinear optics: The case of graphene,” Physical Review B **95**, 035416 (2017).
12. D. A. Smirnova, A. V. Gorbach, I. V. Iorsh, I. V. Shadrivov, and Y. S. Kivshar, “Nonlinear switching with a graphene coupler,” Physical Review B **88**, 045443 (2013).
13. M. Sanderson, Y. S. Ang, S. Gong, T. Zhao, M. Hu, R. Zhong, X. Chen, P. Zhang, C. Zhang, and S. Liu, “Optical bistability induced by nonlinear surface plasmon polaritons in graphene in terahertz regime,” Applied Physics Letters **107**, 203113 (2015).
14. T. Christopoulos, O. Tsilipakos, and E. E. Kriezis, “Low-power bistability in graphene-comprising 3D photonic resonant circuits,” Journal of Applied Physics **122**, 233101 (2017).
15. D. Zhao, S. Ke, Y. Hu, B. Wang, and P. Lu, “Optical bistability of graphene embedded in parity-time-symmetric photonic lattices,” Journal of the Optical Society of America B **36**, 1731–1737 (2019).
16. S. Shareef, Y. S. Ang, and C. Zhang, “Room-temperature strong terahertz photon mixing in graphene,” Journal of the Optical Society of America B **29**, 274–279 (2012).
17. B. Jin, T. Guo, and C. Argyropoulos, “Enhanced third harmonic genera-

tion with graphene metasurfaces," Journal of Optics **19**, 094005 (2017).

18. M. Ghazialsharif, B. H. Fakhar, and M. S. Abrishamian, "Low power third harmonic generation and all-optical switching by graphene surface plasmons," Journal of Optics **21**, 105503 (2019).
19. A. N. Grigorenko, M. Polini, and K. S. Novoselov, "Graphene plasmonics," Nature Photonics **6**, 749–758 (2012).
20. G. V. Naik, V. M. Shalaev, and A. Boltasseva, "Alternative plasmonic materials: Beyond gold and silver," Advanced Materials **25**, 3264–3294 (2013).
21. F. Xia, H. Wang, D. Xiao, M. Dubey, and A. Ramasubramaniam, "Two–dimensional material nanophotonics," Nature Photonics **8**, 899–907 (2014).
22. H. A. Hafez, S. Kovalev, K.-J. Tielrooij, M. Bonn, M. Gensch, and D. Turchinovich, "Terahertz nonlinear optics of graphene: From saturable absorption to high-harmonics generation," Advanced Optical Materials **8**, 1900771 (2019).
23. V. Nikkhah, A. Bakhtafrouz, M. Maddahali, and S. K. Dezaki, "Three-port graphene-based electromagnetic circulator in the terahertz and infrared frequency ranges with a very low loss and wideband response," Journal of the Optical Society of America B **35**, 1754–1763 (2018).
24. N. Kakenov, M. S. Ergoktas, O. Balci, and C. Kocabas, "Graphene based terahertz phase modulators," 2D Materials **5**, 035018 (2018).
25. H. Xu, C. Xiong, Z. Chen, M. Zheng, M. Zhao, B. Zhang, and H. Li, "Dynamic plasmon-induced transparency modulator and excellent absorber-based terahertz planar graphene metamaterial," Journal of the Optical Society of America B **35**, 1463–1468 (2018).
26. K. J. A. Ooi and D. T. H. Tan, "Nonlinear graphene plasmonics," Proceedings of the Royal Society A: Mathematical, Physical and Engineering Sciences **473**, 20170433 (2017).
27. J. D. Cox and F. J. G. de Abajo, "Nonlinear graphene nanoplasmonics," Accounts of Chemical Research **52**, 2536–2547 (2019).
28. J. W. You, Z. Lan, and N. C. Panoiu, "Four-wave mixing of topological edge plasmons in graphene metasurfaces," Science Advances **6**, eaaz3910 (2020).
29. D. M. Ramirez, A. W. Rodriguez, H. Hashemi, J. D. Joannopoulos, M. Soljačić, and S. G. Johnson, "Degenerate four-wave mixing in triply resonant kerr cavities," Physical Review A **83**, 033834 (2011).
30. Z. Lin, T. Alcorn, M. Loncar, S. G. Johnson, and A. W. Rodriguez, "High-efficiency degenerate four-wave mixing in triply resonant nanobeam cavities," Physical Review A **89**, 053839 (2014).
31. T. Christopoulos, O. Tsilipakos, G. Sinatkas, and E. E. Kriezis, "Degenerate four-wave mixing in nonlinear resonators comprising two-dimensional materials: A coupled-mode theory approach," Physical Review B **98**, 235421 (2018).
32. J. Bravo-Abad, S. Fan, S. G. Johnson, J. D. Joannopoulos, and M. Soljacic, "Modeling nonlinear optical phenomena in nanophotonics," Journal of Lightwave Technology **25**, 2539–2546 (2007).
33. H. A. Haus, *Waves and Fields in Optoelectronics* (Prentice-Hall, 1984), 1st ed.
34. T. Gu, N. Petrone, J. F. McMillan, A. van der Zande, M. Yu, G. Q. Lo, D. L. Kwong, J. Hone, and C. W. Wong, "Regenerative oscillation and four-wave mixing in graphene optoelectronics," Nature Photonics **6**, 554–559 (2012).
35. M. Ji, H. Cai, L. Deng, Y. Huang, Q. Huang, J. Xia, Z. Li, J. Yu, and Y. Wang, "Enhanced parametric frequency conversion in a compact silicon-graphene microring resonator," Optics Express **23**, 18679–18685 (2015).
36. Q. Li, M. Davanço, and K. Srinivasan, "Efficient and low-noise single-photon-level frequency conversion interfaces using silicon nanophotonics," Nature Photonics **10**, 406–414 (2016).
37. Y. Zheng, M. Pu, A. Yi, X. Ou, and H. Ou, "4H-SiC microring resonators for nonlinear integrated photonics," Optics Letters **44**, 5784–5787 (2019).
38. T. Christopoulos, O. Tsilipakos, N. Grivas, and E. E. Kriezis, "Coupled-mode-theory framework for nonlinear resonators comprising graphene," Physical Review E **94**, 062219 (2016).
39. W. Suh, Z. Wang, and S. Fan, "Temporal coupled-mode theory and the presence of non-orthogonal modes in lossless multimode cavities," IEEE Journal of Quantum Electronics **40**, 1511–1518 (2004).
40. X. Zeng and M. A. Popović, "Design of triply-resonant microphotonic parametric oscillators based on Kerr nonlinearity," Optics Express **22**, 15837–15867 (2014).
41. X. Cui, W. Zhang, S. Serna, C. Alonso-Ramos, D. Marris-Morini, L. Vivien, J.-J. He, and E. Cassan, "Adjusting third-order nonlinear properties in silicon triply resonant nanobeam cavities," Journal of the Optical Society of America B **35**, 636–642 (2018).
42. L. A. Falkovsky, "Optical properties of graphene and IV-VI semiconductors," Physics-Uspekhi **51**, 887–897 (2008).
43. G. W. Hanson, "Dyadic Green's functions and guided surface waves for a surface conductivity model of graphene," Journal of Applied Physics **103**, 064302 (2008).
44. S. A. Mikhailov and K. Ziegler, "Nonlinear electromagnetic response of graphene: frequency multiplication and the self-consistent-field effects," Journal of Physics: Condensed Matter **20**, 384204 (2008).
45. A. R. Wright, X. G. Xu, J. C. Cao, and C. Zhang, "Strong nonlinear optical response of graphene in the terahertz regime," Applied Physics Letters **95**, 072101 (2009).
46. S. Xie, Y. Zhang, Y. Hu, S. Veilleux, and M. Dagenais, "On-chip fabry-pérot bragg grating cavity enhanced four-wave mixing," ACS Photonics **7**, 1009–1015 (2020).
47. C. Manolatou, M. J. Khan, S. Fan, P. R. Villeneuve, H. A. Haus, and J. D. Joannopoulos, "Coupling of modes analysis of resonant channel add-drop filters," IEEE Journal of Quantum Electronics **35**, 1322–1331 (1999).
48. T. Christopoulos, O. Tsilipakos, G. Sinatkas, and E. E. Kriezis, "On the calculation of the quality factor in contemporary photonic resonant structures," Optics Express **27**, 14505–14522 (2019).
49. T. J. Duffin, M. P. Nielsen, F. Diaz, S. Palomba, S. A. Maier, and R. F. Oulton, "Degenerate four-wave mixing in silicon hybrid plasmonic waveguides," Optics Letters **41**, 155–158 (2015).
50. N. Vermeulen, J. Cheng, J. E. Sipe, and H. Thienpont, "Opportunities for wideband wavelength conversion in foundry-compatible silicon waveguides covered with graphene," IEEE Journal of Selected Topics in Quantum Electronics **22**, 347–359 (2016).
51. Y. Yang, Z. Xu, X. Jiang, Y. He, X. Guo, Y. Zhang, C. Qiu, and Y. Su, "High-efficiency and broadband four-wave mixing in a silicon-graphene strip waveguide with a windowed silica top layer," Photonics Research **6**, 965–970 (2018).
52. H. Hashemi, A. W. Rodriguez, J. D. Joannopoulos, M. Soljačić, and S. G. Johnson, "Nonlinear harmonic generation and devices in doubly resonant Kerr cavities," Physical Review A **79**, 013812 (2009).
53. M. F. Yanik, S. Fan, M. Soljačić, and J. D. Joannopoulos, "All-optical transistor action with bistable switching in a photonic crystal cross-waveguide geometry," Optics Letters **28**, 2506–2508 (2003).
54. Z. Wang, H. Liu, N. Huang, Q. Sun, and J. Wen, "Efficient terahertz-wave generation via four-wave mixing in silicon membrane waveguides," Optics Express **20**, 8920–8928 (2012).
55. B. Jin and C. Argyropoulos, "Nonlinear graphene metasurfaces with advanced electromagnetic functionalities," in *Plasmonics: Design, Materials, Fabrication, Characterization, and Applications XVI,* vol. 10722 (SPIE, 2018), pp. 55 – 62.
56. J. Wu, Y. Yang, Y. Qu, L. Jia, Y. Zhang, X. Xu, S. T. Chu, B. E. Little, R. Morandotti, B. Jia, and D. J. Moss, "2d layered graphene oxide films integrated with micro-ring resonators for enhanced nonlinear optics," Small **16**, 1906563 (2020).
57. Y. Zhang, L. Tao, D. Yi, J.-B. Xu, and H. K. Tsang, "Enhanced four-wave mixing with MoS2 on a silicon waveguide," Journal of Optics **22**, 025503 (2020).

Supplementary material for "Degenerate four-wave mixing in THz with standing-wave graphene resonators"

THOMAS CHRISTOPOULOS,[1,*] ODYSSEAS TSILIPAKOS,[2] AND EMMANOUIL E. KRIEZIS[1]

[1] *School of Electrical and Computer Engineering, Aristotle University of Thessaloniki (AUTH), GR-54124 Thessaloniki, Greece*
[2] *Institute of Electronic Structure and Laser, Foundation for Research and Technology-Hellas (FORTH-IESL), GR-71110 Heraklion, Crete, Greece*
**cthomasa@ece.auth.gr*

Abstract: In this supplementary file, we describe the computational modeling of graphene in the NIR and its surface conductivity. We also include some extra characteristics of the graphene-ribbon waveguide and the respective graphene resonator.

1. Modeling graphene

The linear properties of graphene are modeled through its surface conductivity tensor, which has nonzero elements only for components tangential to graphene. Two distinctive mechanisms contribute in the surface conductivity, namely intraband and interband absorption. In doped graphene, the former is always present while the latter exist only when the interacting photons have enough energy. Commonly, this is not the case in the THz frequency band where the photon energy is a fraction of the eV and thus graphene unique properties solely emerge from the intraband interactions. The equation governing those interactions is [1,2]

$$\sigma_{\text{intra}} = -\frac{je^2\mu_c}{\pi\hbar^2(\omega - j/\tau_{\text{intra}})}\left[1 + \frac{2k_BT}{\mu_c}\ln(1+\exp\{-\mu_c/k_BT\})\right], \tag{S1}$$

where k_B is the Boltzmann's constant, $\hbar$ is the reduced Plank's constant, T is the absolute temperature, τ_{intra} is the relaxation time of the excited electrons and μ_c is the Fermi level of graphene, encapsulating its doping conditions. For nonzero Fermi levels, the temperature dependence is insignificant in room-temperature conditions and the respective term (second term in the bracket) can be dropped. In our work, we chose a typical relaxation time of $\tau_{\text{intra}} =$ 40 ps and an achievable Fermi level of $\mu_c = 0.3$ eV. Under these conditions, the linear surface conductivity of graphene is plotted in Fig. S1 between 4 and 6 THz. The strongly negative values of surface conductivity's imaginary part indicate the possibility to support surface plasmon polaritons.

Graphene has also a highly nonlinear response, which is of Kerr type. When only intraband interactions are involved, the nonlinear response can be estimated by the closed-form expression [3]

$$\sigma_3 = j\frac{3e^4\upsilon_F^2}{32\omega^3\hbar^2\mu_c}, \tag{S2}$$

where $\upsilon_F \approx c_0/300$ is the Fermi velocity in graphene. Note the inverse proportionality (with the third power) between the nonlinear surface conductivity and the frequency. Also note that Eq. (S2) allows the calculation of the only independent nonzero element of the 4th rank nonlinear surface conductivity tensor of graphene. The nonzero elements of the tensor are those allowing solely for tangential interactions and reduce to 8 for a graphene sheet oriented in parallel to any of the coordinate planes.

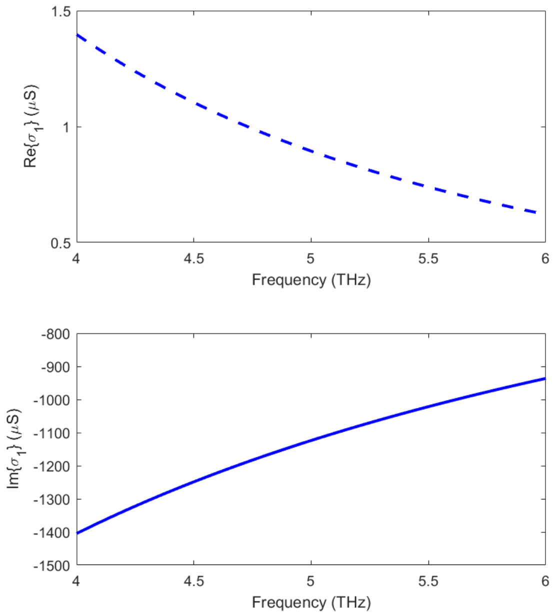

Fig. S1. Graphene surface conductivity versus frequency (FIR).

2. GSP waveguide characteristics

Following the frequency-dependent model of graphene surface conductivity, one can calculate through full-wave simulations the dispersion diagrams of a free-standing graphene ribbon of width $w = 1$ μm. Such a calculation is important in order to have an estimation of the mode confinement and the accompanied resistive losses of the mode. The results are shown in Fig. S2. Note that in the calculation, one must keep in mind that both material and waveguide dispersion are considered. Therefore, it is revealed that higher frequencies result in more confined modes with lower resistive losses. Nevertheless, single-mode operation with sufficient distance from the next supported mode is essential in resonant systems, where higher order modes can potentially be excited through the discontinuity in the coupling regions. Thus, relatively low frequencies are highly desirable and subsequently chosen in this work.

In another perspective, we fix the frequency at 5 THz and examine the effective index with respect to the ribbon width w. The results of Fig. S3 reveal that larger ribbons exhibit lower resistive losses and lower mode confinement as well. With the former being desirable and the latter not, it is rational to choose the ribbon width at $w = 1$ μm for this work, as a compromise between the two trends.

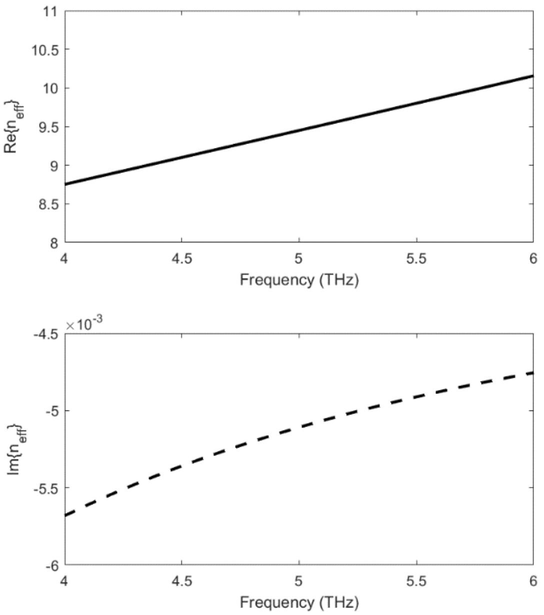

Fig. S2. Effective refractive index of the guided surface plasmon mode on a free-standing $w = 1$ μm graphene ribbon versus frequency (NIR).

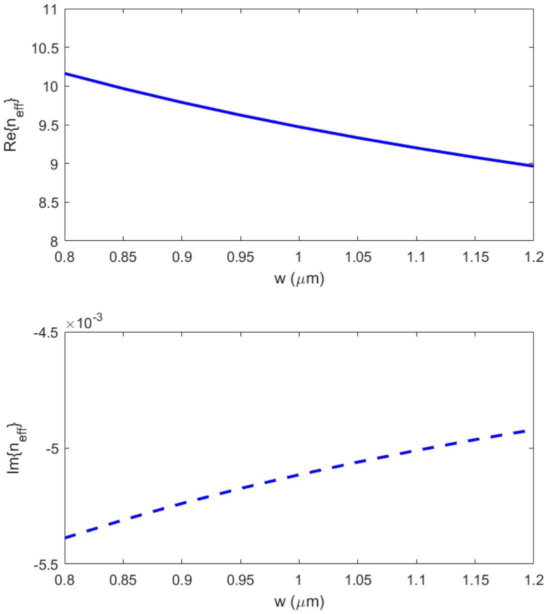

Fig. S3. Effective index of the guided surface plasmon mode on the graphene ribbon versus ribbon's width w at a fixed frequency, $f = 5$ THz.

3. Standing-wave resonator characteristics

Finally, the resonator characteristics are examined with the respective results presented in Fig. S4. Specifically, we examine how the width of the ribbon affects the resonance frequencies and the respective intrinsic quality factors of the three consecutive modes used in the manuscript (calculated with 3D FEM simulations –see the points in the figure– with the consideration of graphene's strongly dispersive nature). A smooth change in all tree resonance frequencies is observed (left panel of Fig. S3), reflecting the equally smooth change in $\mathrm{Re}\{n_{\mathrm{eff}}\}$ (Fig. S2) and the inverse proportionality relation between the resonance frequencies and the real part of the effective index [Fabry-Pérot cavity resonance frequencies, $f = mc_0/2\mathrm{Re}\{n_{\mathrm{eff}}\}L$]. Finally, from the right panel of Fig. R3, presenting the intrinsic quality factors, it can be inferred that resistive loss dominates over radiation: Despite radiation loss raises due to the lower mode confinement, the intrinsic Q-factor reveals overall lower losses (thus exhibiting higher values), owing to the weaker resistive loss contribution as w increases (cf. Fig. R2). Note that for the modes presented, the resonance order is retained ($m = 8$ for the pump wave, $m = 9$ for the signal wave, and $m = 7$ for the idler wave).

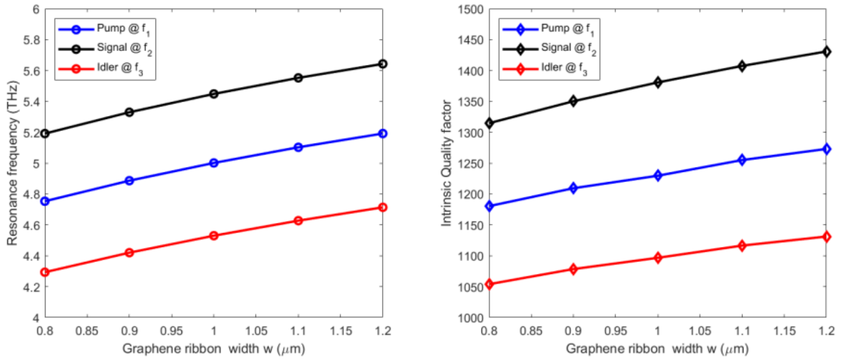

Fig. S4. Left: Resonance frequency of the graphene-ribbon standing-wave resonator versus ribbon's width w. Right: Intrinsic quality factor of the respective modes versus ribbon's width w. Pump corresponds to resonant mode of order $m = 8$, signal to mode $m = 9$, and idler to mode $m = 7$.

References

1. L. A. Falkovsky, "Optical properties of graphene and IV-VI semiconductors," Physics-Uspekhi **51**, 887–897 (2008).
2. G. W. Hanson, "Dyadic Green's functions and guided surface waves for a surface conductivity model of graphene," Journal of Applied Physics **103**, 064302 (2008).
3. S. A. Mikhailov and K. Ziegler, "Nonlinear electromagnetic response of graphene: frequency multiplication and the self-consistent-field effects," Journal of Physics: Condensed Matter **20**, 384204 (2008).